ADVANCED FUNCTIONAL MATERIALS
www.afm-journal.de

Shape-Assisted 2D MOF/Graphene Derived Hybrids as Exceptional Lithium-Ion Battery Electrodes

Kolleboyina Jayaramulu, Deepak P. Dubal,* Andreas Schneemann, Václav Ranc, Cecilia Perez-Reyes, Jana Stráská, Štěpán Kment, Michal Otyepka, Roland A. Fischer,* and Radek Zbořil**

Herein, a novel polymer-templated strategy is described to obtain 2D nickel-based MOF nanosheets using $Ni(OH)_2$, squaric acid, and polyvinylpyrrolidone (PVP), where PVP has a dual role as a structure-directing agent, as well as preventing agglomeration of the MOF nanosheets. Furthermore, a scalable method is developed to transform the 2D MOF sheets to Ni_7S_6/graphene nanosheet (GNS) heterobilayers by in situ sulfidation using thiourea as a sulfur source. The Ni_7S_6/GNS composite shows an excellent reversible capacity of 1010 mAh g^{-1} at 0.12 A g^{-1} with a Coulombic efficiency of 98% capacity retention. The electrochemical performance of the Ni_7S_6/GNS composite is superior not only to nickel sulfide/graphene-based composites but also to other metal disulfide–based composite electrodes. Moreover, the Ni_7S_6/GNS anode exhibits excellent cycle stability (≈95% capacity retention after 2000 cycles). This outstanding electrochemical performance can be attributed to the synergistic effects of Ni_7S_6 and GNS, where GNS serves as a conducting matrix to support Ni_7S_6 nanosheets while Ni_7S_6 prevents restacking of GNS. This work opens up new opportunities in the design of novel functional heterostructures by hybridizing 2D MOF nanosheets with other 2D nanomaterials for electrochemical energy storage/conversion applications.

1. Introduction

Energy storage and conversion are major global challenges. Due to their finite nature and issues related to climate change and environmental pollution, it is necessary to reduce fossil fuel consumption and shift toward renewable and environmentally friendly energy sources.[1] Energy storage devices are essential for storing energy produced by renewable energy sources, for instance in electric vehicles or for their integration into the power grid. Li-ion batteries (LiB) are promising high capacity energy storage systems for these applications, but significantly suffer from a low charge/discharge rate compared with other important electrochemical storage devices, such as supercapacitors.[2–8] Nevertheless, precious metal sulfides have been reported as promising LiB anode materials, based on the "conversion reaction". However, these metal sulfides performance is limited by poor kinetics, conductivity, and capacitance because of their dissolution as polysulfides in the electrolyte, leading to electrode polarization.[9–11] In order to overcome these critical challenges, new synthesis methods have been developed to control the size, significant surface area, and morphology of metal sulfides.[8]

Recently, hybrid porous crystalline metal–organic frameworks (MOFs) have been proposed for various energy related applications, such as supercapacitors, catalysis, sensing, and gas storage/separation, owing to their unique properties like highly ordered, nanoporous, tunable, and functional pores.[12–21] Indeed, their large surface area and precise structural organization allows for the adsorption of

Dr. K. Jayaramulu, Dr. A. Schneemann, Prof. R. A. Fischer
Chair of Inorganic and Metal-Organic Chemistry
Department of Chemistry and Catalysis Research Centre
Technical University of Munich
85748 Garching, Germany
E-mail: jaya.kolleboyina@tum.de; roland.fischer@tum.de

Dr. K. Jayaramulu, Dr. V. Ranc, C. Perez-Reyes, J. Stráská, Dr. Š. Kment, Prof. M. Otyepka, Prof. R. Zbořil
Regional Centre of Advanced Technologies and Materials
Faculty of Science
Palacky University
Šlechtitelů 27, 783 71 Olomouc, Czech Republic
E-mail: radek.zboril@upol.cz

Dr. D. P. Dubal
School of Chemistry
Physics and Mechanical Engineering
Queensland University of Technology (QUT)
2 George Street, Brisbane 4001, Queensland, Australia
E-mail: deepak.dubal@qut.edu.au, dubaldeepak2@gmail.com

Dr. A. Schneemann
Sandia National Laboratories
7011 East Avenue, Livermore 94551, CA, USA

The ORCID identification number(s) for the author(s) of this article can be found under https://doi.org/10.1002/adfm.201902539.

DOI: 10.1002/adfm.201902539

ions from an electrolyte, which is beneficial to generate high capacitance. However, the application of pristine MOF materials for electrochemical applications is largely hindered by their poor electrical conductivity and chemical stability.[18,22–24] Numerous methods have been reported to improve the conductivity, for example by integration of MOF materials with external carbonaceous layers, quantum dots, graphene, polyaniline, or guest molecules, and by the preparation of MOF-derived hybrids.[25–30] Nevertheless, the use of bulk MOF crystals and polymer binder decreases the effective surface area and would turn active metal sites within the hybrids inaccessible. Although, recent developments in 2D MOFs have produced remarkable advances in various applications compared to traditional 3D MOF because of their ultrathin thickness, large surface area, high surface to volume ratios, and accessible active metal sites.[2,31–43]

Herein, we report a general, scalable approach for the in situ synthesis of a heterolayered nickel sulfide/graphene composite, and its use as an anode material in Li-ion batteries. The composite is obtained by the conversion of a hybrid of nickel-based metal–organic framework nanosheets, using thiourea as a sulfide source. The 2D nickel-based metal framework $[Ni(C_4O_4)(H_2O)_2]_n$ is obtained from $Ni(OH)_2$ and squaric acid ($H_2C_4O_4$), in the presence of the structure-directing agent polyvinylpyrrolidone (PVP) under hydrothermal conditions at 120 °C (denoted as 2D NiMOF). The use of $Ni(OH)_2$ as a nickel source eliminates byproducts containing chloride and nitride anions. Chlorides tend to increase the corrosivity of the reaction mixture and nitrates require special attention in high volume synthesis, due to the exothermic nature of the MOF synthesis.

2. Results and Discussion

2.1. Polymer-Templated 2D MOF Nanosheets

The synthesis of 2D MOF nanosheets still remains challenging, because the growth of MOF crystals needs to be suppressed to the nanometer scale only along one direction. In our work, PVP is employed as an effective template, favoring the formation of ultrathin nickel-squarate MOF nanosheets. In contrast, the absence of PVP in the reaction gives millimeter-sized green crystals (for complete details see the Experimental Section and Figure S1 in the Supporting Information). Single crystal X-ray diffraction (SXRD) studies confirm a crystal structure with the general formula $[Ni(C_4O_4)(H_2O)_2]_n$ isoreticular to previously reported manganese, zinc, and cobalt squarates.[44] In the crystal structure, each nickel ion is coordinated to four different squarates along the equatorial plane to form 2D $[Ni(C_4O_4)]_n$ sheets. Therefore, each Ni^{2+} is bridged to 12 different Ni^{2+} centers via the tetradentate $C_4O_4^{2-}$. In the apical positions, the Ni^{2+} is coordinated to two water molecules, resulting in an octahedral coordination environment (Figure S2, Supporting Information). Phase purity of the resultant bulk product is confirmed through powder X-ray diffraction (PXRD) measurements (Figure S3, Supporting Information). When PVP is employed in the hydrothermal synthesis of $[Ni(C_4O_4)(H_2O)_2]_n$, a green colored powder is produced. The powder sample is thoroughly characterized by elemental analysis, Fourier transform infrared (FT-IR) spectroscopy, Raman spectroscopy, and powder XRD analysis measurements. Interestingly, the powder XRD pattern reveals, the obtained powder is isostructural with the prepared single crystals (**Figure 1**a).[36] Further, Raman spectroscopy of the powder confirms the presence of Ni—O bonds and imaging reveals a homogenous distribution of the Ni—O bond throughout the sample (Figure 1b). Scanning electron microscopy (SEM) suggests the existence of nanosheets and their assembly into microspheres (Figure 1c–e; Figure S4, Supporting Information). Transmission electron microscopy (TEM) of 2D NiMOF reveals that nanosheet morphology and the lateral size of each sheet is around 100–200 nm (Figure 1f–h). A typical high-angle annular dark-field (HAADF) TEM image of 2D NiMOF powder shows a uniform and homogenous distribution of C, O, and Ni over the whole nanosheet (Figure 1i–m). Finally, atomic force microscopy (AFM) confirms a thickness of a representative nanosheet of around 18.5 nm (Figure S5, Supporting Information). The FT-IR spectrum of bulk and 2D NiMOF indicates similar structural features and coordination environments (Figure S6, Supporting Information). Further, microscopy reveals that PVP also helps to stabilize the as-synthesized MOF nanosheets as shown in **Scheme 1**a. The importance of PVP as a structure-directing agent is established through synthesis of 2D MOF nanosheets with varying concentration of reactants under similar reaction conditions (the complete experimental details are provided in Table S1, Supporting Information). Note, that without the addition of PVP, large (3D) single crystals of $[Ni(C_4O_4)(H_2O)_2]_n$ are obtained under similar conditions. In order to gain information on the formation mechanism of the nanosheets, field-emission SEM (FESEM) measurements were conducted after different reaction times (Figure S7, Supporting Information). Interestingly, the evolution of the morphology can be monitored. After 1 h of reaction, microcubes are formed, and if the reaction is continued further, these cubes are reduced in size to microplates (3 h) which then turn into spherical agglomerates of nanoplates (6 h). Further reaction leads to the formation of spherical nanotape agglomerates (12 h) and finally to spherical agglomerates of 2D nanosheets. These experiments explicitly suggest that PVP acts as both capping agent and structure-directing agent in the formation of ultrathin nanosheets. The surface area calculated from nitrogen adsorption measured at 77 K using Brunauer–Emmett–Teller (BET) equation is 67 $m^2\ g^{-1}$ (Figure S8a, Supporting Information). Moreover, the obtained 2D NiMOF shows significant N_2 and CO_2 uptake (10 and 26 $cm^3\ g^{-1}$ STP, respectively) at room temperature (Figures S8b and S9, Supporting Information). Contrary, the bulk NiMOF crystals shows nonporous behaviour with a typical type-II adsorption isotherm, suggesting improvement of textural features of the nanosheets.

2.2. Synthesis of Heterostructures of 2D NiMOF and Graphene

Few layer graphene was prepared through liquid-phase exfoliation of graphite flakes (complete experimental details and structural data are provided in the Supporting information and Figure S10, Supporting Information). The obtained 2D graphene layers were combined with the 2D NiMOF layers

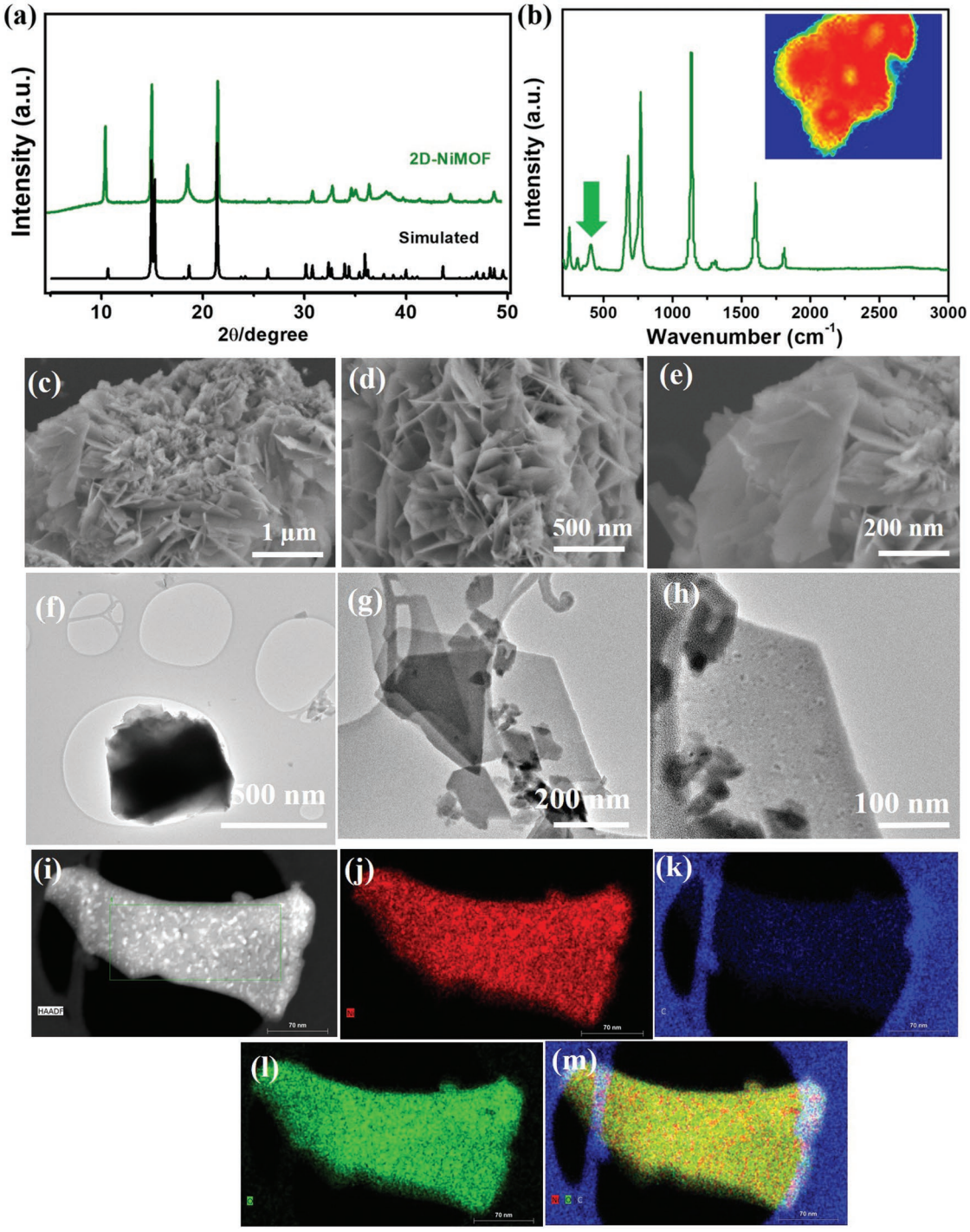

Figure 1. a) Powder XRD patterns of 2D NiMOF (green) and pattern of 3D $[Ni(C_4O_4)(H_2O)_2]_n$ (black); b) Raman spectra of 2D NiMOF, inset shows Raman map of Ni—O bond distributed throughout sample; micrographs of 2D NiMOF c–e) SEM images depicting nanosheets with diameters of 200–100 nm; f–h) TEM images showing ultrathin 2D MOF layers; i–m) EDS chemical mapping confirms homogenous elemental distribution of corresponding elements: i) HAADF image, j) nickel, k) carbon, and l) oxygen; m) combined distribution of Ni, C, and oxygen elements.

to synthesize hetero 2D structures under solvothermal conditions at 120 °C (experimental details in the Supporting Information). The powder XRD of the resulting 2D hybrid material shows high intensity reflections which are all matching with the pattern of 2D NiMOF, confirming structural integrity of the starting material. In a typical sulfidation reaction, the hybrid 2D NiMOF/graphene nanosheet (GNS) stacks are converted into a 2D nickel sulfide/GNS heterostructure under solvothermal conditions at 180 °C using thiourea as a sulfur source in presence of water/ethanol (Scheme 1b). The 2D NiMOF has a dual role, as the nickel precursor and as a sacrificial template. The PXRD pattern of the product (denoted as Ni_7S_6/GNS) has all

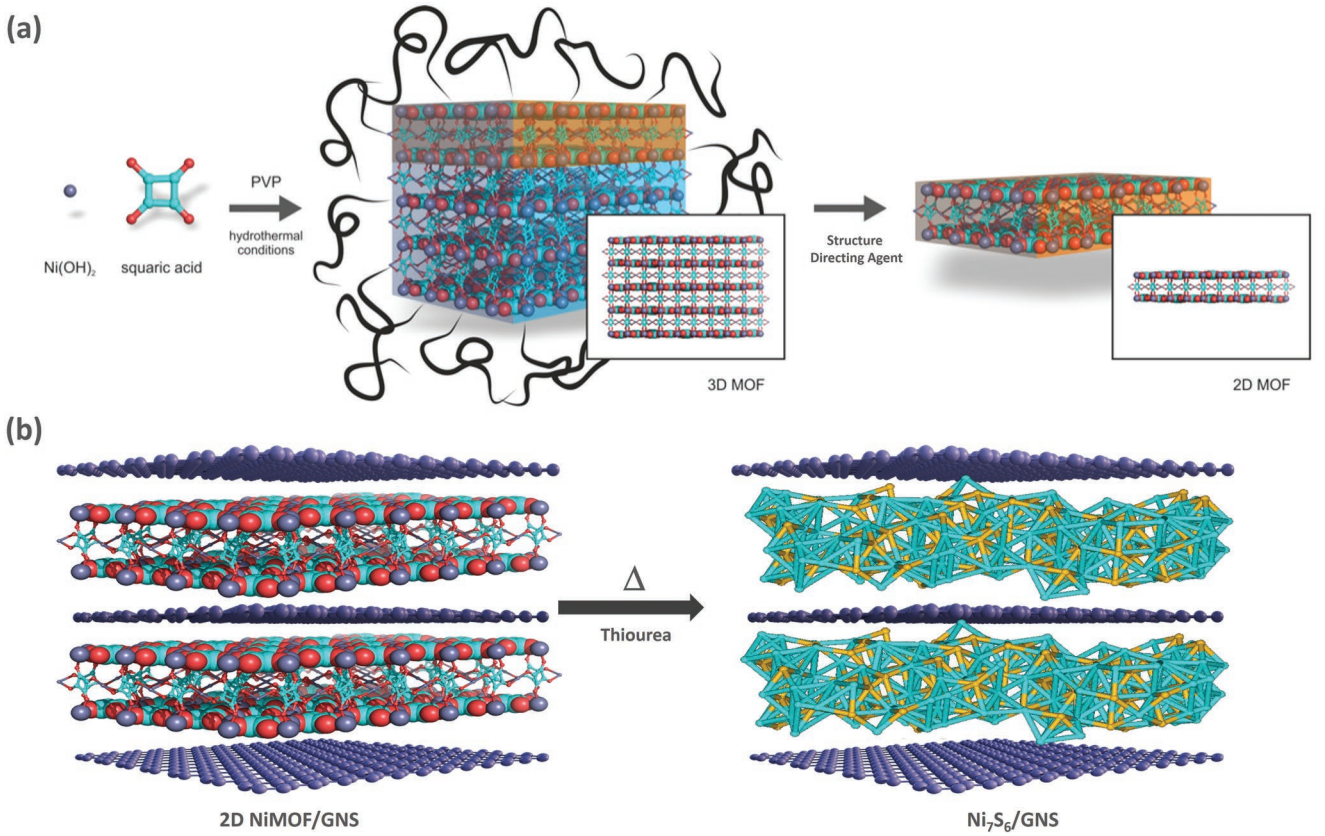

Scheme 1. a) Schematic illustration of the formation of 2D NiMOF layers from 3D MOF. Based on experimental evidence, PVP acts as a structure-directing agent. b) In situ preparation of heterobilayer hybrids of 2D graphene with nickel sulfide from 2D NiMOF using thiourea under solvothermal conditions.

reflections that correspond to the Ni_7S_6 phase (JCPDS Card No. 14-0364) (**Figure 2**a). Raman analysis of Ni_7S_6 /GNS shows the typical signals of graphene at 1340 (D band) and 1593 cm^{-1} (G band), the former is attributed to sp^3 carbon and the latter to graphitic (sp^2) carbon (Figure 2b). Moreover, it confirms that during solvothermal reaction conditions some defects are formed in the graphene due to vacancies and bonding disorders. Raman imaging of the Ni—S bond reveals homogeneous distribution throughout the sample, suggesting full conversion of the precursors.

The XPS survey spectrum exhibits sharp signals corresponding to Ni, S, and C, respectively, which is in accordance with the composition of Ni_7S_6/GNS (Figure S11, Supporting Information). The deconvolution of the S 2p reveals two peaks at 162.5 and 163.6 eV, which belong to S $2p_{3/2}$ and S $2p_{1/2}$, as well as a broad satellite peak at a binding energy of 168.9 eV (Figure 2c). The Ni$2p_{3/2}$ can be resolved into two peaks as 853.2 and 856.4 eV, indicating the presence of divalent and trivalent Ni species (Figure 2d).[45] TEM measurements exhibit the formation of a 2D sheet morphology with lateral sizes of sheets between 50 and 100 nm (**Figure 3**a–c). Further, high-resolution TEM (HRTEM) images of the hybrid show that within the morphology, nanosheets of both the graphene and nickel sulfide layers are present. Additionally, HAADF-TEM mapping shows uniform distribution of nickel, sulfide, and carbon through the sample, confirming homogeneity of the prepared material (Figure 3d–g). Therefore, the resultant heterocomposite is constructed of nickel sulfide nanosheets intercalated in between graphene nanosheets with significant graphitic behavior.

2.3. Li-Ion Battery Analysis of Ni_7S_6/GNS as Anode Material

The unique construction of graphene nanosheets intercalated between Ni_7S_6 nanosheets of Ni_7S_6/GNS makes it a promising heterobilayer composite for electrochemical storage applications. The electrochemical performance of the Ni_7S_6/GNS nanocomposite was assessed as an anode material for Li-ion batteries in a potential range of 0.01–2.5 V (vs Li/Li^+). The cyclic voltammetry (CV) curves for Ni_7S_6/GNS were recorded at 0.2 mV s^{-1} and are presented in Figure S12 in the Supporting Information. Notably, the Ni_7S_6/GNS anode displays reproducible CV curves with distinct reduction and oxidation peaks. During the first cathodic scan, the Ni_7S_6/GNS anode shows two small peaks at ≈1.75 and ≈1.3 V, which are ascribed to the incorporation of lithium ions into Ni_7S_6 (according to Equation (1)),[46] and the transformation of Ni_7S_6 to Li_2S and Ni (Equation (2)), respectively. The peaks observed at 1.0 V and below can be assigned to the formation of a solid-electrolyte interphase (SEI) film on the surface of the electrodes, which vanishes in the following cycle

$$Ni_7S_6 + xLi^+ + xe^- \leftrightarrow Li_xNi_7S_6 \quad (1)$$

$$Ni_7S_6 + 12Li^+ + 12e^- \leftrightarrow 7Ni + 6Li_2S \quad (2)$$

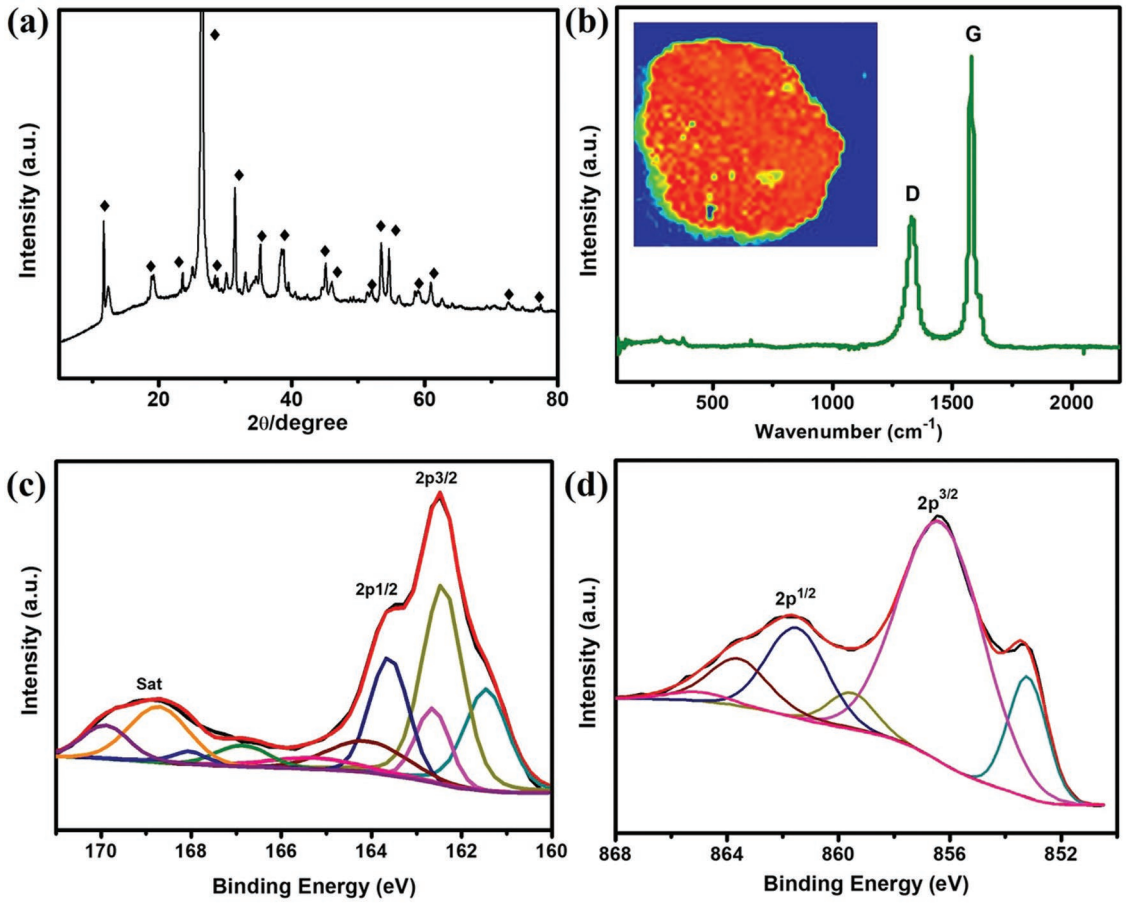

Figure 2. a) Powder XRD pattern of GNS/Ni_7S_6 heterobilayer reflections belonging to the Ni_7S_6 phase (JCPDS Card No. 14-0364) are marked with a diamond, b) Raman spectrum of GNS/Ni_7S_6 showing D and G bands and inset showing homogeneous distribution of the D and G band throughout the sample. High-resolution c) S 2p and d) Ni 2p XPS spectrum.

During further cathodic scanning, a small amount of lithium is stored in the interphase between Ni particles and Li_2S, as well as in defect sites.[47] In the reverse anodic scan, the part of lithium, which is stored in the Ni/Li_2S interphase and the defects, is removed in two steps, which are represented by the dual peaks at 1.05 and 1.45 V. Another broad and intense peak is observed at 2.1 V and is assigned to the oxidation of nickel to nickel sulfide (according to Equation (2)). Notably, there is no big loss of area underneath the CV curves in the successive cycles, proving good capacity retention of the composites. These reversible redox peaks suggest good cycling stability of the Ni_7S_6/GNS electrode. According to the CV measurements, it is worth noting that the composites have excellent durability and all redox peaks are well-matched to charge–discharge plateaus (see **Figure 4**a). Discharge/charge voltage profiles for Ni_7S_6/GNS were recorded at 0.12 A g^{-1} within the potential range between 0.01 and 2.5 V (vs Li/Li^+). The 1st specific discharge capacity was 1596 mAh g^{-1}, while the 1st specific charge capacity was 998 mAh g^{-1} and corresponds to a Coulombic efficiency of 62%. The initial irreversible capacity can be attributed to the decomposition of the electrolyte and formation of SEI, and the irreversible reactions between Ni_7S_6 and Li^+.[48,49] Two small voltage plateaus appeared at 1.5 and 1.16 V, which can be assigned to the prelithiation (Equation (1)) and reduction of Ni_7S_6 (Equation (2)), respectively, while the plateaus below 0.7 V can be assigned to the formation of SEI. The small plateaus observed in the 1st charge cycle at around 1.2 and 2.1 V can be associated with the SEI and Ni oxidation, respectively. The discharge capacities in the 2nd and 10th cycles were found to be 1066 and 989 mAh g^{-1}, respectively, and the charge capacities were 984 and 958 mAh g^{-1}, respectively, which corresponds to Coulombic efficiencies of 92.3% and 96.9%, respectively. The high Coulombic efficiencies after the 1st cycle demonstrate the positive effect of graphene on the maintenance of the Ni_7S_6 redox reactions. The stability of the voltage profiles in the first 10 cycles further confirmed that the nanocomposite underwent stable lithium insertion and extraction, and that graphene wrapping of Ni_7S_6 nanoparticles stabilized the redox process by providing a conductive support that can maintain the engagement of the active materials in the redox processes. The rate performance of Ni_7S_6/GNS nanocomposite was accessed by recording charge-discharge (CD) curves at different current densities (see Figure S12 in the Supporting Information). The specific capacities were found to be 1010, 493, 315, and 231 mAh g^{-1} at 10th cycle of current densities of 0.12, 1, 5, and 10 A g^{-1}, respectively, with Coulombic efficiency of around 98% as seen from Figure 4b. The excellent rate performance of Ni_7S_6/GNS can be assigned to the ability of good adhesion between graphene

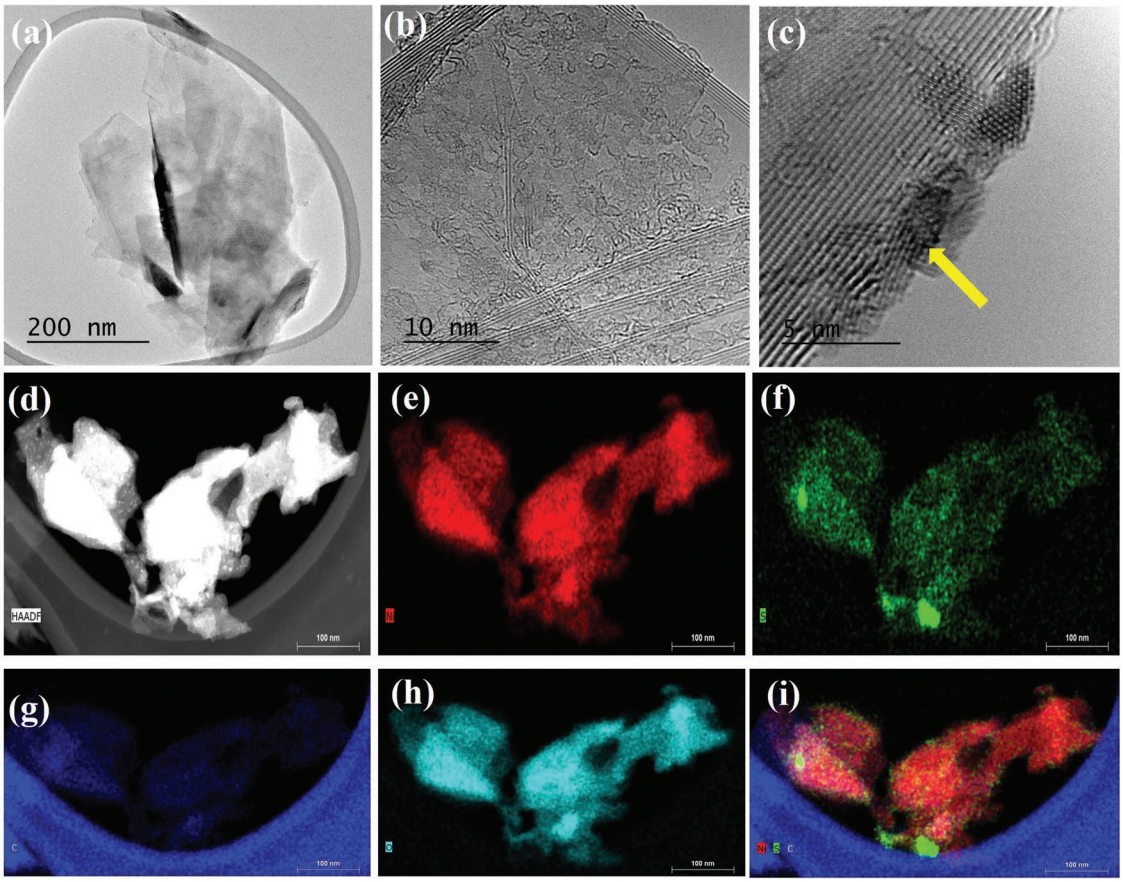

Figure 3. a–c) HRTEM micrograph of GNS/Ni_7S_6 showing heterolayers of graphene and Ni_7S_6. In particular, (c) confirms the stacking of the layers in an alternating fashion; EDS elemental mapping d) HAADF image e) nickel, f) sulfur, g) carbon, h) oxygen, and i) combination of all corresponding elements reveals homogenous distribution of all elements throughout the sample.

and Ni_7S_6 nanosheets, which reduce the electron and Li^+ diffusion paths and enhance the electrode kinetics. In addition, the Ni_7S_6/GNS nanocomposite allows for greater electrolyte access to the electrochemically active sites, which further improves electrode kinetics. Moreover, graphene wrapping forms a conductive network that boosts the electrode conductivity, thus improving the rate performance.

In order to investigate the charge transfer kinetics of the Ni_7S_6/GNS nanocomposite, the charges associated with semi-infinite diffusion controlled and capacitive (includes the sum of pseudocapacitance originated from rapid surface redox charge-transfer processes and non-Faradaic EDLC process) reactions were determined. In this context, the cyclic voltammetry curves for the Ni_7S_6/GNS hybrid were recorded at different scan rates (Figure 4c). It is commonly accepted that the current response in CV curves obeys a power-law relationship with the sweep rate[49]

$$i = ab^{v} \tag{3}$$

where "i" is the current (mA), v is the potential sweep rate (mV s^{-1}), and a and b are arbitrary coefficients. Whereas $b = 0.5$ signifies that the current is controlled by semi-infinite linear diffusion, and $b = 1$ indicates that the current is surface-controlled (capacitive).[50] The value of b can be estimated by determining the slope of the plot of log(i, mA) versus log(v, mV s^{-1}). From Figure 4d, it can be observed that the b-values calculated in the potential range 0.1–1.5 V (vs Li/Li^+) lie between 0.79 and 0.84, indicating that the major charge contribution is from surface capacitive reactions. Specially, the b-values (around 0.84) of the surface reaction related to the bond of −graphene−C−O−Li are close to 1, corresponding to the special electrochemical behavior of pseudocapacitance.[51] To further quantify the capacitive charge contribution, it is assumed that the total charge stored at a fixed potential is the sum of capacitive charge (k_1v), and diffusion-controlled contribution ($k_2v^{-1/2}$), which can be expressed as follows

$$i = k_1v + k_2v^{1/2} \tag{4}$$

where k_1 and k_2 are constants, which can be determined by plotting $i/v^{1/2}$ versus $v^{1/2}$ and measuring slope (k_1) and the y-axis intercept (k_2), respectively. Inserting the values of k_1 and k_2 in Equation (4), one can separately quantify surface capacitive and diffusion-controlled contributions. Figure 4e shows the comparison of calculated capacitive charges (shaded) with the experimental currents (solid line), suggesting about 66% of the total current of the Ni_7S_6/GNS hybrid electrode is contributed by the capacitive mechanism at 1 mV s^{-1}. Thus, the result suggests that the Ni_7S_6/GNS electrode is mainly pseudocapacitive

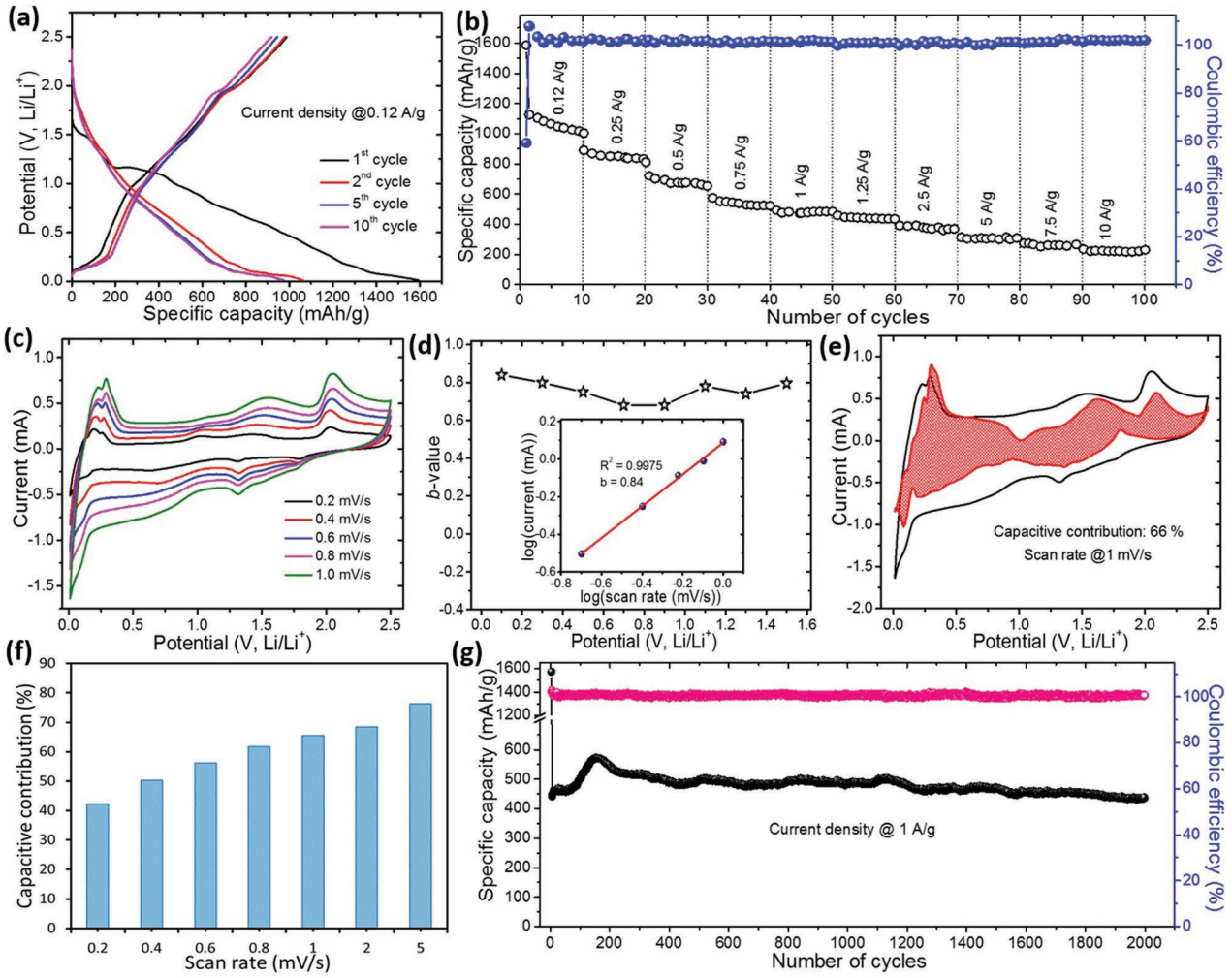

Figure 4. Li-ion battery testing of Ni_7S_6/GNS composite anode materials: a) Galvanostatic charge/discharge profiles recorded for first 10 cycles at 0.12 A g^{-1}. b) Rate performance of composite electrodes at different current densities with corresponding Coulombic efficiency. c) Cyclic voltammetry curves measured at different scanning rates from 0.2 to 1 mV s^{-1} in potential range of 0.01–2.5 V (vs Li/Li^+). d) Plot of *b*-value versus potential in the voltage range of 0.1–1.5 V (vs Li/Li^+), inset shows the log (*i*) versus log (scan rate). e) CV response at a scan rate of 1 mV s^{-1} with the shaded area representing the capacitive contribution to the total current. f) Variation of capacitive charge contribution at different scan rates. g) Long-term cycle stability over 2000 cycles at 1 A g^{-1}.

in nature. It is further observed that the capacitive charge contribution increases with scan rates from 0.2 to 5 mV s^{-1} reaching 77% at 5 mV s^{-1} as shown in Figure 4f.

Long-term cycling stability is a key parameter to determine the feasibility of materials to be used in LiBs. The life cycle test of Ni_7S_6/GNS was assessed at a current density of 1 A g^{-1} and results are presented in Figure 4g. The Ni_7S_6/GNS nanocomposite experienced an irreversible capacity loss in the 1st cycle due to SEI formation, and capacity fading in the initial few cycles. However, this trend was reversed, and the capacity started to increase from 439 mAh g^{-1} (7th cycle) and reached 579 mAh g^{-1} until the 150th cycle. The increase in capacity over cycling was previously observed for CoO, and was ascribed to the slow reaction of irreversible Li_2O that was formed during the 1st discharge.[52] Another possibility is that during the insertion/extraction of lithium ions, the composite generated more defects, which could be used as active sites for lithium ion storage.[53] The graphene present in Ni_7S_6/GNS nanocomposite helps to maintain the integrity of the active material after its disintegration. It also mitigates polysulfide dissolution and enhances electron and ionic transport.[54] After 150 cycles, the capacity gradually starts to decrease and reaches 481 and 421 mAh g^{-1} after 1000 and 2000 cycles, respectively, which is slightly less than that of the 7th cycle (439 mAh g^{-1}), suggesting excellent cycling stability. The decrease in capacity with cycles after the activation period can be associated with the loss in contact of the active material and a disintegration mechanism of metal sulfide (Ni_7S_6). Notably, a high Coulombic efficiency of more than 98% was maintained over 2000 cycles, suggesting excellent reversibility of the Ni_7S_6/GNS hybrid material. The electrochemical performances of Ni_7S_6/GNS engineered in this work is not only better than those of other phase nickel sulfide/graphene composites but also superior to those of other metal disulfide–based composite electrodes.[46,55–60] For example, a Ni_3S_2/N-doped graphene composite showed a reversible capacity of 720 mAh g^{-1} at 50 mA g^{-1} and slowly increased up

Table 1. Comparison of specific capacities and cycling stability of Ni_7S/GNS nanocomposite with the values reported in the literature.

Materials	Specific capacity [mAh g^{-1}]	Cycling stability	Refs.
2D MOF-derived Ni_7S_6/graphene	1010 at 120 mA g^{-1}	95% after 2000 cycles	Present work
Graphene-wrapped Ni_7S_6 nanoprisms	834 at 70 mA g^{-1}	74% at 70 mA g^{-1} after 200 cycles	[61]
Ni_3S_4–N-doped graphene	1300 at 140.9 mA g^{-1}	98.85% at 140.9 mA g^{-1} after 100 cycles	[46]
Carbon nanotube/Ni_3S_4 composite	845 at 60 mA g^{-1}	87% at 300 mA g^{-1} after 100 cycles	[57]
Ni_3S_2@C-RGO	608 at 100 mA g^{-1}	83% at 100 mA g^{-1} after 500 cycles	[58]
NiS_2/graphene composite	1010 at 100 mA g^{-1}	80% at 500 mA g^{-1} after 1000 cycles	[60]
rGO@Co_9S_8	944 at 545 mA g^{-1}	40% at 545 mA g^{-1} after 500 cycles	[59]
CoS_2@G	800 at 50 mA g^{-1}	Increases to 900 mAh g^{-1} at 50 mA g^{-1} after 100 cycles	[61]
MnS/graphene composite	854 at 50 mA g^{-1}	58% at 50 mA g^{-1} after 500 cycles	[62]
MnS/N–S-doped graphene	763.5 at 100 mA g^{-1}	62% at 1000 mA g^{-1} after 2000 cycles	[63]
2D MoS_2	1008 at 200 mA g^{-1}	85% at 200 mA g^{-1} after 50 cycles	[47]

to 809 mAh g^{-1} after 150 cycles.[53] The NiS/graphene composite delivered an initial reversible capacity of 976 mAh g^{-1} at 59 mA g^{-1} and retained the capacity of 887 mAh g^{-1} after 60 cycles.[55] The detailed comparison of present results with literature is provided in **Table 1**.

The structural and morphological changes of the Ni_7S_6/GNS hybrid material were investigated by ex situ XRD, Raman, and SEM analysis. The ex situ XRD patterns of Ni_7S_6/GNS electrodes recorded at 1st discharge (0.01 V), 1st charge (2.5 V), and after the 100th and 2000th discharge cycles were compared with fresh electrode material (see **Figure 5**a). It is evidenced that the low intensity reflections completely disappeared in the 1st discharge/charge cycle while the two strong diffraction peaks observed at 26.9° and 55° are recovered, suggesting partial-reversibility of the material. Moreover, some new peaks were observed after 100th and 2000th cycle that corresponds to the Ni_7S_6 phase (JCPDS: 014-0364), suggesting that Ni_7S_6 maintains its original crystal structure with

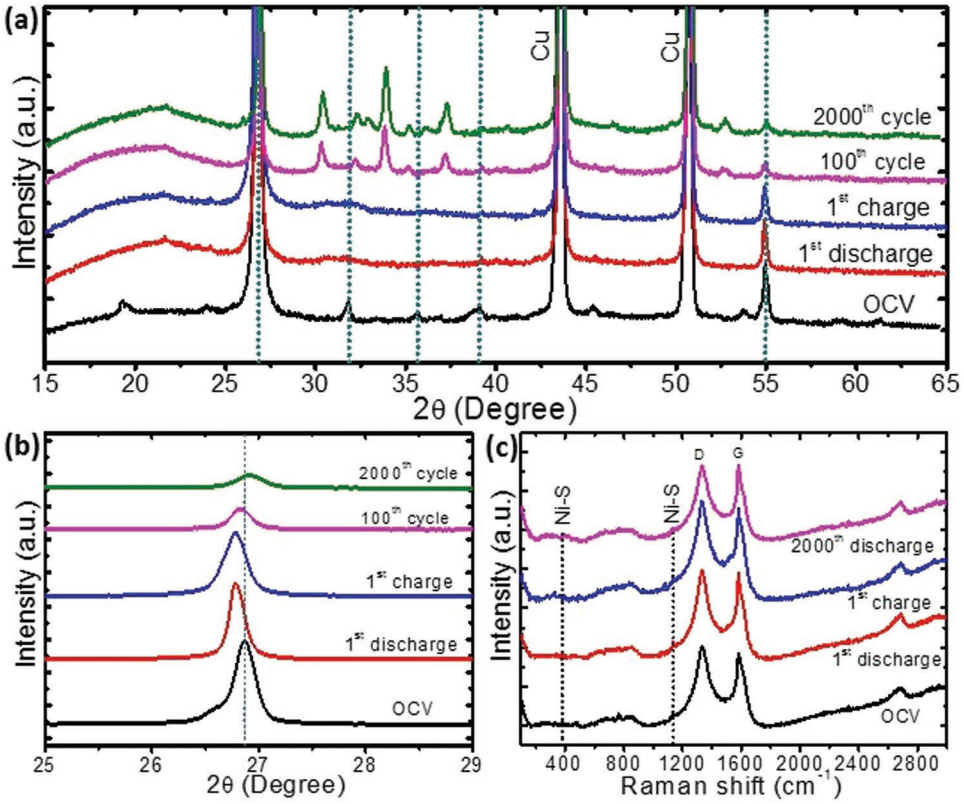

Figure 5. a,b) Ex situ XRD patterns of electrodes recorded for 1st discharge (0.01 V), 1st charge (2.5 V), after 100th and 2000th charge/discharge cycles, and compared with noncycled electrode with their magnified parts, respectively. c) Raman spectra measured for cycled electrodes (1st discharge, 1st charge, and 100th and 2000th charge/discharge cycles).

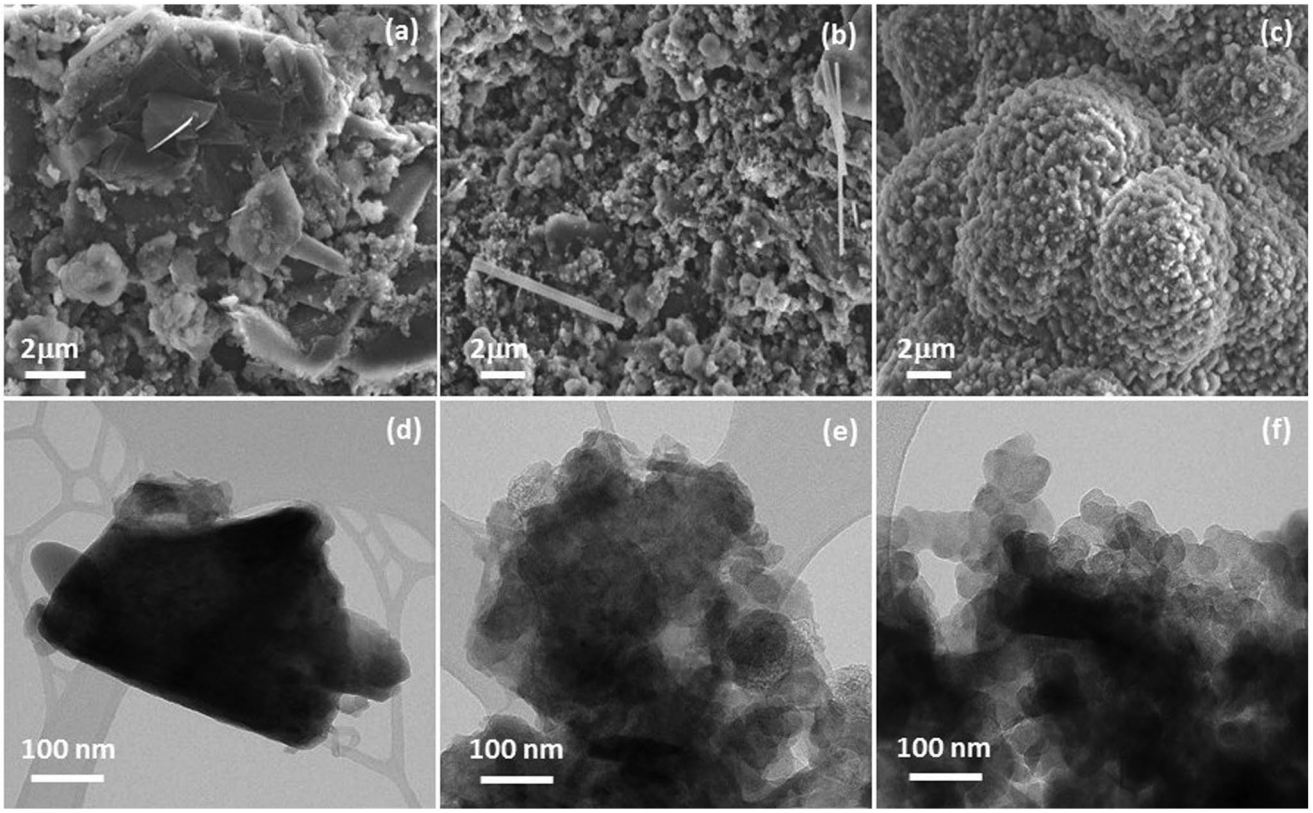

Figure 6. a–c) SEM images and d–f) TEM images of Ni_7S_6/GNS electrode after 1st discharge, and 100th and 2000th charge/discharge cycle, suggesting transformation of the morphology in the beginning, which was maintained for the next more than 2000 cycles.

some additional crystal orientations along different planes during discharge/charge cycles. These new reflections with the original strong reflections (26.9° and 55°) are retained for the subsequent cycles, suggesting that the newly formed orientations are extremely stable over long charge/discharge cycles. The magnified XRD patterns of the characteristic reflection of Ni_7S_6 at 26.9° (Figure 5b) suggest small displacement of the peak position, which indicates increase/decrease in the interplanar distance of Ni_7S_6 sheets during discharging/charging cycles. The Ni_7S_6/GNS electrodes were further characterized by ex situ Raman spectroscopy as shown in Figure 5c. For as-synthesized Ni_7S_6/GNS electrode (OCV), characteristic bands at around 374 and 1100 cm^{-1} are observed, which correspond to vibration modes of nickel sulfide (Ni—S) bonds. There is no significant difference in the Raman spectra of cycled and fresh Ni_7S_6/GNS electrodes, suggesting excellent structural stability of the Ni_7S_6/GNS electrode. This could be attributed to the unique 2D nanostructures of the Ni_7S_6/GNS where the MOF-derived Ni_7S_6 nanosheets are wrapped with graphene nanosheets, which provide an ion-buffering reservoir during the charge/discharge process. The positions and peak intensities of the D and G bands correspond to graphene nanosheets and remain at the same positions after several charging/discharging cycles. The effect of charge/discharge processes on surface morphology of Ni_7S_6/GNS was investigated by SEM and TEM analysis (**Figure 6**). After the 1st discharge cycle, no significant change in the nanosheet-like morphology of Ni_7S_6/GNS was observed while after 100 cycles, the nanostructure is transformed into irregular and very small particles as can be seen from Figure 6b,e. Nevertheless, it is interesting to note that the nanoparticulate architecture was subsequently conserved for more than 2000 charge/discharge cycles (Figure 6c,f). This observation suggests that after a few initial discharge cycles, Ni_7S_6 converts into a nanoparticle-like morphology with another dominant orientation (crystal planes), which is strongly supported by the XRD results. Moreover, this nanoparticle architecture is uniformly covered by the graphene nanosheets, so that GNS cannot be seen in SEM but can be confirmed from Raman spectra.

3. Conclusion

In summary, we demonstrated a facile method for the preparation of nickel squarate–based 2D $[Ni(C_4O_4)(H_2O)_2]_n$ nanosheets by simple reaction of $Ni(OH)_2$ with squaric acid in the presence of the polymer PVP. The polymer acts as a structure-directing agent to control the morphology of the 3D MOF to obtain 2D MOF nanosheets. In addition, we reported the intercalation of the nanosheets in between GNS, followed by their conversion to 2D Ni_7S_6/GNS nanosheets under solvothermal condition in presence of thiourea. The spectroscopic and microscopic measurements reveal that the obtained hybrids have nickel sulfide layers intercalated in between graphene layers. As a proof-of-concept application, the obtained Ni_7S_6/GNS heterocomposite nanosheets were tested for electrochemical lithium storage

applications. The hybrid shows significant reversible capacity and remarkable, enhanced rate-capability along with exceptional cyclic stability. These superior electrochemical lithium storage properties, can be attributed to the following reasons: 1) the synergistic effects of Ni_7S_6 and graphene nanosheets, where GNS serves as a perfect matrix to support Ni_7S_6 nanosheets while Ni_7S_6 prevents restacking of GNS. 2) The excellent electrical conductivity of GNS and the MOF-derived porous Ni_7S_6 nanostructure accelerates the charge transfer and the volume change of Ni_7S_6/GNS is efficiently suppressed during the repetitive lithiation/delithiation process. 3) In addition, the Ni_7S_6/GNS hybrid electrode offers a large number of channels for the diffusion of lithium ions and allows access of the electrolyte. Therefore, Ni_7S_6/GNS composite does not only deliver a high reversible specific capacity with excellent cyclic stability, but also exhibit significantly enhanced rate-capability. It is expected that this kind of novel hetero 2D nanosheets have promise for application in solar cells, catalysis, and photocatalysis.

Supporting Information

Supporting Information is available from the Wiley Online Library or from the author.

Acknowledgements

K.J. and D.P.D. contributed equally to this work. D.P.D. acknowledges the Queensland University of Technology and Australian Research Council (ARC) for the Future Fellowship (FT180100058). A.S. acknowledges the Deutsche Forschungsgemeinschaft (German Research Foundation) for a postdoctoral fellowship (SCHN 1539/1-1). The authors thank O. Tomanec (Palacký University) for HRTEM measurements, and M. Petr (Palacký University) for measurement of XPS data. The authors gratefully acknowledge support by the Catalysis Research Centre at Technische Universität München (TUM) for analytical support. The authors also gratefully acknowledge, the assistance provided by the Research Infrastructure NanoEnviCz, supported by the Ministry of Education, Youth and Sports of the Czech Republic under Project No. LM2015073. The authors also gratefully acknowledge support by the Operational Programme Research, Development and Education – European Regional Development Fund, Project Nos. CZ.02.1.01/0.0/0.0/15_003/0000416 and CZ.02.1.01/0.0/0.0/16_019/0000754 of the Ministry of Education, Youth and Sports of the Czech Republic.

Conflict of Interest

The authors declare no conflict of interest.

Keywords

2D metal–organic frameworks, energy storage, graphene, heterobilayer hybrids, Li-ion battery, nickel sulfide

Received: March 27, 2019
Revised: July 1, 2019
Published online: July 23, 2019

[1] V. Dusastre, L. Martiradonna, *Nat. Mater.* **2017**, *16*, 15.
[2] X. Xu, W. Liu, Y. Kim, J. Cho, *Nano Today* **2014**, *9*, 604.
[3] D. Di Lecce, R. Verrelli, J. Hassoun, *Green Chem.* **2017**, *19*, 3442.
[4] D. P. Dubal, D. R. Patil, S. S. Patil, N. R. Munirathnam, P. Gomez-Romero, *ChemSusChem* **2017**, *10*, 4163.
[5] X. Liu, J.-Q. Huang, Q. Zhang, L. Mai, *Adv. Mater.* **2017**, *29*, 1601759.
[6] Y. An, H. Fei, G. Zeng, L. Ci, S. Xiong, J. Feng, Y. Qian, *ACS Nano* **2018**, *12*, 4993.
[7] Y. An, H. Fei, G. Zeng, X. Xu, L. Ci, B. Xi, S. Xiong, J. Feng, Y. Qian, *Nano Energy* **2018**, *47*, 503.
[8] Y. Tian, Y. An, J. Feng, *ACS Appl. Mater. Interfaces* **2019**, *11*, 10004.
[9] Y. Zhao, L. P. Wang, M. T. Sougrati, Z. Feng, Y. Leconte, A. Fisher, M. Srinivasan, Z. Xu, *Adv. Energy Mater.* **2017**, *7*, 1601424.
[10] P. Geng, S. Zheng, H. Tang, R. Zhu, L. Zhang, S. Cao, H. Xue, H. Pang, *Adv. Energy Mater.* **2018**, *8*, 1703259.
[11] J. Zhao, Y. Zhang, Y. Wang, H. Li, Y. Peng, *J. Energy Chem.* **2018**, *27*, 1536.
[12] S. Dissegna, K. Epp, W. R. Heinz, G. Kieslich, R. A. Fischer, *Adv. Mater.* **2018**, *30*, 1704501.
[13] S. Furukawa, J. Reboul, S. Diring, K. Sumida, S. Kitagawa, *Chem. Soc. Rev.* **2014**, *43*, 5700.
[14] L. Jiao, Y. Wang, H. L. Jiang, Q. Xu, *Adv. Mater.* **2018**, *30*, 1703663.
[15] W. Wang, X. Xu, W. Zhou, Z. Shao, *Adv. Sci.* **2017**, *4*, 1600371.
[16] W. Xuan, C. Zhu, Y. Liu, Y. Cui, *Chem. Soc. Rev.* **2012**, *41*, 1677.
[17] Q. Yang, Q. Xu, H. L. Jiang, *Chem. Soc. Rev.* **2017**, *46*, 4774.
[18] S. L. Li, Q. Xu, *Energy Environ. Sci.* **2013**, *6*, 1656.
[19] C. Mu, F. Xu, W. Lei, *Prog. Chem.* **2007**, *19*, 1345.
[20] K. Yang, G. Zhou, Q. Xu, *RSC Adv.* **2016**, *6*, 37506.
[21] L. F. Chen, Q. Xu, *Science* **2017**, *358*, 304.
[22] L. Wang, Y. Han, X. Feng, J. Zhou, P. Qi, B. Wang, *Coord. Chem. Rev.* **2016**, *307*, 361.
[23] Y. Horiuchi, T. Toyao, M. Takeuchi, M. Matsuoka, M. Anpo, *Phys. Chem. Chem. Phys.* **2013**, *15*, 13243.
[24] A. A. Olajire, *Renewable Sustainable Energy Rev.* **2018**, *92*, 570.
[25] Q.-L. Zhu, Q. Xu, *Chem. Soc. Rev.* **2014**, *43*, 5468.
[26] P. Freund, I. Senkovska, S. Kaskel, *ACS Appl. Mater. Interfaces* **2017**, *9*, 43782.
[27] B. Zhu, R. Zou, Q. Xu, *Adv. Energy Mater.* **2018**, *8*, 1801193.
[28] A. Indra, T. Song, U. Paik, *Adv. Mater.* **2018**, *30*, 1705146.
[29] K. Jayaramulu, D. P. Dubal, B. Nagar, V. Ranc, O. Tomanec, M. Petr, K. K. R. Datta, R. Zbořil, P. Gomez-Romero, R. A. Fischer, *Adv. Mater.* **2018**, *30*, 1705789.
[30] Y. An, Z. Zhang, H. Fei, S. Xiong, B. Ji, J. Feng, *ACS Appl. Mater. Interfaces* **2017**, *9*, 12400.
[31] K. Jayaramulu, J. Masa, D. M. Morales, O. Tomanec, V. Ranc, M. Petr, P. Wilde, Y. T. Chen, R. Zbořil, W. Schuhmann, R. A. Fischer, *Adv. Sci.* **2018**, *5*, 1801029.
[32] P. Amo-Ochoa, L. Welte, R. González-Prieto, P. J. Sanz Miguel, C. J. Gómez-García, E. Mateo-Martí, S. Delgado, J. Gómez-Herrero, F. Zamora, *Chem. Commun.* **2010**, *46*, 3262.
[33] M. Zhao, Y. Huang, Y. Peng, Z. Huang, Q. Ma, H. Zhang, *Chem. Soc. Rev.* **2018**, *47*, 6267.
[34] F. Cao, M. Zhao, Y. Yu, B. Chen, Y. Huang, J. Yang, X. Cao, Q. Lu, X. Zhang, Z. Zhang, C. Tan, H. Zhang, *J. Am. Chem. Soc.* **2016**, *138*, 6924.
[35] S. Sakaida, K. Otsubo, O. Sakata, C. Song, A. Fujiwara, M. Takata, H. Kitagawa, *Nat. Chem.* **2016**, *8*, 377.
[36] X. Wang, C. Chi, K. Zhang, Y. Qian, K. M. Gupta, Z. Kang, J. Jiang, D. Zhao, *Nat. Commun.* **2017**, *8*, 14460.
[37] S. Zhao, Y. Wang, J. Dong, C.-T. He, H. Yin, P. An, K. Zhao, X. Zhang, C. Gao, L. Zhang, J. Lv, J. Wang, J. Zhang, A. M. Khattak,

N. A. Khan, Z. Wei, J. Zhang, S. Liu, H. Zhao, Z. Tang, *Nat. Energy* **2016**, *1*, 16184.
[38] R. Makiura, S. Motoyama, Y. Umemura, H. Yamanaka, O. Sakata, H. Kitagawa, *Nat. Mater.* **2010**, *9*, 565.
[39] T. Rodenas, I. Luz, G. Prieto, B. Seoane, H. Miro, A. Corma, F. Kapteijn, F. X. Llabrés i Xamena, J. Gascon, *Nat. Mater.* **2015**, *14*, 48.
[40] Y. Peng, Y. Li, Y. Ban, H. Jin, W. Jiao, X. Liu, W. Yang, *Science* **2014**, *346*, 1356.
[41] Q. Lu, M. Zhao, J. Chen, B. Chen, C. Tan, X. Zhang, Y. Huang, J. Yang, F. Cao, Y. Yu, J. Ping, Z. Zhang, X.-J. Wu, H. Zhang, *Small* **2016**, *12*, 4669.
[42] D. J. Ashworth, J. A. Foster, *J. Mater. Chem. A* **2018**, *6*, 16292.
[43] D. Feng, T. Lei, M. R. Lukatskaya, J. Park, Z. Huang, M. Lee, L. Shaw, S. Chen, A. A. Yakovenko, A. Kulkarni, J. Xiao, K. Fredrickson, J. B. Tok, X. Zou, Y. Cui, Z. Bao, *Nat. Energy* **2018**, *3*, 30.
[44] S. Neeraj, M. L. Noy, C. N. R. Rao, A. K. Cheetham, *Solid State Sci.* **2002**, *4*, 1231.
[45] K. Jayaramulu, J. Masa, O. Tomanec, D. Peeters, V. Ranc, A. Schneemann, R. Zbořil, W. Schuhmann, R. A. Fischer, *Adv. Funct. Mater.* **2017**, *27*, 1700451.
[46] N. Mahmood, C. Zhang, Y. Hou, *Small* **2013**, *9*, 1321.
[47] U. K. Sen, S. Mitra, *ACS Appl. Mater. Interfaces* **2013**, *5*, 1240.
[48] C. Xu, Y. Zeng, X. Rui, N. Xiao, J. Zhu, W. Zhang, J. Chen, W. Liu, H. Tan, H. H. Hng, Q. Yan, *ACS Nano* **2012**, *6*, 4713.
[49] D. P. Dubal, K. Jayaramulu, R. Zbořil, R. A. Fischer, P. Gomez-Romero, *J. Mater. Chem. A* **2018**, *6*, 6096.
[50] D. P. Dubal, P. Gomez-Romero, *Mater. Today Energy* **2018**, *8*, 109.
[51] V. Augustyn, J. Come, M. A. Lowe, J. W. Kim, P.-L. Taberna, S. H. Tolbert, H. D. Abruña, P. Simon, B. Dunn, *Nat. Mater.* **2013**, *12*, 518.
[52] J.-S. Do, C.-H. Weng, *J. Power Sources* **2005**, *146*, 482.
[53] J. Zhu, Y. Li, S. Kang, X.-L. Wei, P. K. Shen, *J. Mater. Chem. A* **2014**, *2*, 3142.
[54] G. Zhou, D.-W. Wang, F. Li, L. Zhang, N. Li, Z.-S. Wu, L. Wen, G. Q. Lu, H.-M. Cheng, *Chem. Mater.* **2010**, *22*, 5306.
[55] H. Geng, S. F. Kong, Y. Wang, *J. Mater. Chem. A* **2014**, *2*, 15152.
[56] A. A. AbdelHamid, X. Yang, J. Yang, X. Chen, J. Y. Ying, *Nano Energy* **2016**, *26*, 425.
[57] P. Fan, H. Liu, L. Liao, J. Fu, Z. Wang, G. Lv, L. Mei, H. Hao, J. Xing, J. Dong, *RSC Adv.* **2017**, *7*, 49739.
[58] P. Yu, L. Wang, J. Wang, D. Zhao, C. Tian, L. Zhao, H. Yu, *RSC Adv.* **2016**, *6*, 48083.
[59] H. Wang, S. Lu, Y. Chen, L. Han, J. Zhou, X. Wu, W. Qin, *J. Mater. Chem. A* **2015**, *3*, 23677.
[60] Q. Chen, W. Chen, J. Ye, Z. Wang, J. Y. Lee, *J. Power Sources* **2015**, *294*, 51.
[61] J. Xie, S. Liu, G. Cao, T. Zhu, X. Zhao, *Nano Energy* **2013**, *2*, 49.
[62] D. Chen, H. Quan, G.-S. Wang, L. Guo, *ChemPlusChem* **2013**, *78*, 843.
[63] B. Liu, Z. Liu, D. Li, P. Guo, D. Liu, X. Shang, M. Lv, D. He, *Appl. Surf. Sci.* **2017**, *416*, 858.